

## Engineering Carrier Effective Masses in Ultrathin Quantum Wells of IrO<sub>2</sub>

Jason K. Kawasaki,<sup>1,2,3,4,\*</sup> Choong H. Kim,<sup>5,6</sup> Jocienne N. Nelson,<sup>2</sup> Sophie Crisp,<sup>2</sup> Christian J. Zollner,<sup>7</sup>

Eric Biegenwald,<sup>3</sup> John T. Heron,<sup>3</sup> Craig J. Fennie,<sup>7</sup> Darrell G. Schlom,<sup>1,3</sup> and Kyle M. Shen<sup>1,2,†</sup>

<sup>1</sup>Kavli Institute at Cornell for Nanoscale Science, Cornell University, Ithaca, New York 14853, USA

<sup>2</sup>Laboratory for Atomic and Solid State Physics, Cornell University, Ithaca, New York 14853, USA

<sup>3</sup>Department of Materials Science and Engineering, Cornell University, Ithaca, New York 14853, USA

<sup>4</sup>Department of Materials Science and Engineering, University of Wisconsin, Madison, Wisconsin 53706, USA

<sup>5</sup>Center for Correlated Electron Systems, Institute for Basic Science, Seoul, Korea

<sup>6</sup>Department of Physics and Astronomy, Seoul National University, Seoul, Korea

<sup>7</sup>Department of Applied and Engineering Physics, Cornell University, Ithaca, New York 14853, USA

 (Received 26 February 2018; revised manuscript received 9 May 2018; published 25 October 2018)

The carrier effective mass plays a crucial role in modern electronic, optical, and catalytic devices and is fundamentally related to key properties of solids such as the mobility and density of states. Here we demonstrate a method to deterministically engineer the effective mass using spatial confinement in metallic quantum wells of the transition metal oxide IrO<sub>2</sub>. Using a combination of *in situ* angle-resolved photoemission spectroscopy measurements in conjunction with precise synthesis by oxide molecular-beam epitaxy, we show that the low-energy electronic subbands in ultrathin films of rutile IrO<sub>2</sub> have their effective masses enhanced by up to a factor of 6 with respect to the bulk. The origin of this strikingly large mass enhancement is the confinement-induced quantization of the highly nonparabolic, three-dimensional electronic structure of IrO<sub>2</sub> in the ultrathin limit. This mechanism lies in contrast to that observed in other transition metal oxides, in which mass enhancement tends to result from complex electron-electron interactions and is difficult to control. Our results demonstrate a general route towards the deterministic enhancement and engineering of carrier effective masses in spatially confined systems, based on an understanding of the three-dimensional bulk electronic structure.

DOI: [10.1103/PhysRevLett.121.176802](https://doi.org/10.1103/PhysRevLett.121.176802)

Quantum confinement is an essential ingredient for exploring the fundamental physics of two-dimensional electron systems and for modern technologies as devices become scaled down to the atomically thin limit. In the simplest picture, confinement in the out-of-plane direction results in quantized two-dimensional subbands. In nearly all so-called quantum well systems investigated to date (e.g., semiconductor quantum wells [1–3] and noble metals [4–6]), the in-plane effective mass is, at most, only weakly dependent on the subband index. The ability to deterministically engineer the effective mass or density of states of each subband could have implications for technological applications that depend on quantum confinement, such as quantum cascade lasers [7], tunnel diodes [8], and photocatalysts [9].

Transition metal oxides offer inherent advantages for devices based on quantum confinement, owing to their unparalleled range of exotic electronic and magnetic properties and to their high carrier densities and the tunability of their electronic structure [10]. Rutile IrO<sub>2</sub> is a technologically important transition metal oxide, exhibiting a large spin Hall effect for spin injection and detection [11], and is an efficient catalyst for the oxygen evolution reaction [12]. In these applications, the magnitude of the spin Hall angle and the catalytic activity depend sensitively

on the effective mass, and therefore it is highly desirable to be able to tune the effective mass in a deterministic way.

Here, we demonstrate the ability to enhance the subband effective masses of atomically thin films of IrO<sub>2</sub> grown by oxide molecular-beam epitaxy (MBE) by up to a factor of 6, as investigated by angle-resolved photoemission spectroscopy (ARPES). We show that the effective masses can be deliberately engineered by applying quantum confinement to a material with a highly nonparabolic, three-dimensional dispersion, thereby quantizing the values of  $k_z$  by selecting the number of monolayers in the material. This approach can be broadly applied to a wide class of other functional materials. In contrast to other mechanisms for tuning the effective mass, such as epitaxial strain [13] and crystallographic orientation [14], which produce changes on the order of tens of percents, the mechanism we report here originates specifically from quantum confinement and produces changes up to a factor of 6. This behavior can be predicted based on a simple model of momentum discretization.

Figure 1 presents an overview of the structural and transport properties of our ultrathin IrO<sub>2</sub> films, grown by MBE on (110)-oriented TiO<sub>2</sub> substrates. In addition to the sharp 110 and 220 Bragg reflections, we observe sharp and

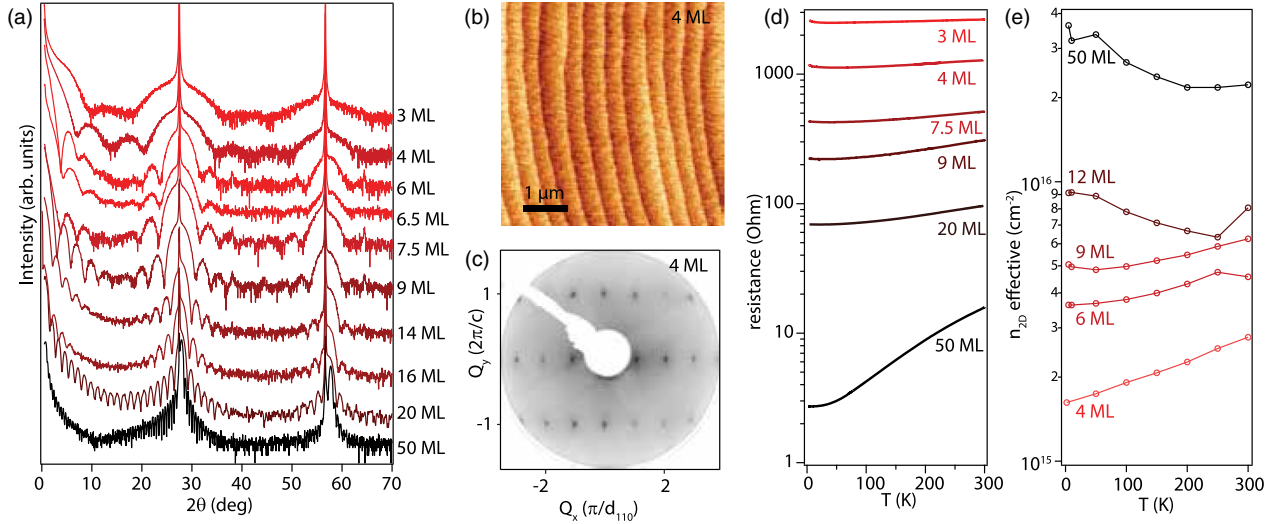


FIG. 1. Structural and transport characteristics of ultrathin  $\text{IrO}_2$  thin films grown on  $(110)$   $\text{TiO}_2$ . (a) X-ray diffraction  $\theta - 2\theta$  scans ( $\text{Cu } K\alpha$ ). (b) Atomic force microscopy topograph of a 4 monolayer (ML) thick film, with step heights corresponding to 1 ML. (c) Low-energy electron diffraction ( $h\nu = 150$  eV) pattern of the 4 ML film showing a sharp  $(1 \times 1)$  pattern and indicating a well atomically ordered surface. (d) Resistance versus temperature measured along  $[001]$ , showing retained metallicity for all films. (e) Effective 2D carrier density (defined as inverse of the Hall coefficient  $1/R_{Hq}$ , where  $q =$  fundamental charge) versus temperature, showing hole dominated transport.

persistent finite thickness (Kiessig) fringes over nearly the entire range of measured angles, indicating atomically smooth surfaces and interfaces. X-ray rocking curves exhibit full width at half maxima on the order of 20–35 arc sec, comparable to the substrate. Together with the step-and-terrace morphology revealed by atomic force microscopy [Fig. 1(b)] and the sharp  $(1 \times 1)$  low-energy electron diffraction pattern [Fig. 1(c)], these measurements establish the high structural quality of our ultrathin films. Further details of growth and characterization are provided in the Supplemental Material [15] and in Refs. [19,20].

Temperature-dependent resistivity measurements reveal metallic behavior ( $dR/dT > 0$ ) for all films down to 3 ML thickness [Fig. 1(d)]. Below 40 K, the 3 and 4 ML films show a slight upturn in resistance below 40 K. This metallicity in the atomically thin limit is already quite remarkable in that the majority of ultrathin transition metal oxide thin films (e.g.,  $\text{La}_{1-x}\text{Sr}_x\text{MnO}_3$  [21],  $\text{SrRuO}_3$  [22]) show thickness-driven metal-insulator transitions below approximately 4 unit cells. The 50 ML sample exhibits a residual resistivity of only  $\rho_{4K} = 4 \mu\Omega\text{cm}$ , the lowest of any  $\text{IrO}_2$  films reported to date [23–25], establishing the high quality of these samples. Hall effect measurements [Fig. 1(e)] indicated sheet carrier (holelike) densities in the range of  $10^{15}$ – $10^{16} \text{ cm}^{-2}$  ( $n_{3D} \sim 10^{22} \text{ cm}^{-3}$ ). This number should, however, be treated only as approximate, due to the complex multiband nature of  $\text{IrO}_2$ , which is also evidenced in the nontrivial temperature dependence. The effective three-dimensional carrier density sharply decreases for films with thickness less than 10 ML, indicating the strong effects of quantum confinement (Supplemental Material [15]).

In Fig. 2(a) we show *in situ* ARPES measurements through the zone center  $(0,0)$  along  $k_x \parallel [1\bar{1}0]$ , measured using He  $I\alpha$  ( $h\nu = 21.2$  eV) photons. Along this cut, the bulk limit (50 ML) is characterized by highly dispersive holelike (band max above  $E_F$ ) and electronlike ( $\approx -1.5$  eV band bottom) bands centered at  $(0,0)$  that are well described by density functional theory (DFT) calculations that include spin-orbit coupling (Supplemental Material [15] and Ref. [19]). The bulk Fermi surface is highly three dimensional [Fig. 2(b)], and at this photon energy the ARPES measurement corresponds approximately to a slice at a constant perpendicular momentum of  $k_z = (0.76 \pm 0.05)\pi/d_{110}$  [19].

As the film thickness is decreased, additional electronlike bands become readily apparent and evolve with film thickness. These additional states represent subbands generated by quantum confinement in the out-of-plane direction. In Fig. 2(a) the symbols represent the fitted subband dispersions as extracted from energy dispersion curve (EDC) fits near the band bottom and momentum distribution curve (MDC) fits near the Fermi energy. Measurement using a different photon energy,  $h\nu = 40.8$  eV (He  $II\alpha$ ), yields nearly identical dispersions, confirming the two-dimensional character of these subbands. The corresponding Fermi surface is nearly two-dimensional [Fig. 2(e)].

In Fig. 2(d) we plot the thickness evolution of the subband bottoms (circles), together with a fit (lines) to the Bohr-Sommerfeld quantization rule [4,26],  $2k_z(E)L + \phi(E) = 2\pi n$ . Here  $k_z(E)$  is the component of crystal momentum along the surface normal (from our GGA + SO calculation for bulk; see Supplemental Material [15]),  $L = Nd_{110}$  is the

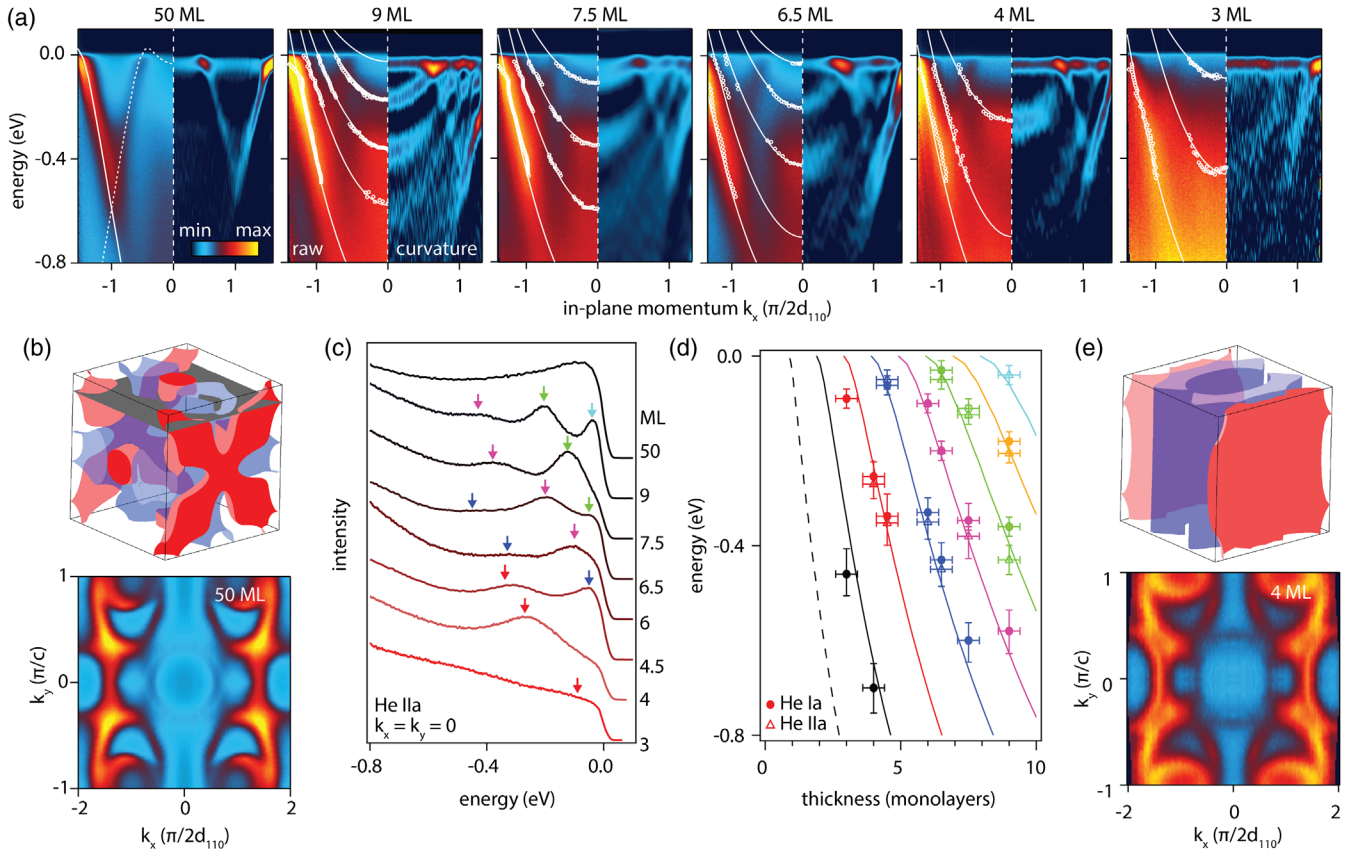


FIG. 2. ARPES measurements of metallic quantum well states. (a) Cuts along  $k_x \parallel [1\bar{1}0]$  through  $(0,0)$  for films 50–4 ML thick (measured using He  $I\alpha$ ). The left side of each plot is the raw data and the right side is the second derivative  $(-\partial^2 I / \partial E^2)$ , i.e., the curvature) of the raw data. Symbols denote EDC and MDC fits. Solid and dotted curves for 50 ML are the bulk GGA + SO calculation [including zone folding at the  $(110)$  surface [19]], curves for 9 ML and thinner are empirical guides to the eye. (b) Three-dimensional GGA + SO Fermi surface (upper) and ARPES measured slice at constant  $k_z$  through Fermi surface (lower) in the bulklike limit (50 ML). The constant  $k_z = 0.76\pi/d_{110}$  slice is denoted by the gray plane through the three-dimensional Fermi surface, as determined from fitting to a free-electronlike model of final states [19]. (c) Energy dispersion curves (measured using He  $II\alpha$ ) through  $(0,0)$  tracking the evolution of quantum well states. (d) Measured energy of the subband bottom versus film thickness (circles) and fit to the phase accumulation model (curves). Fits to the  $n = 2$  subband for the 3 and 4 ML thick films (black data points) are extrapolated from EDC fits in the region near  $k_{\parallel} = 0$ . (e) Schematic Fermi surface in the 2D limit (upper) and measured Fermi surface for the 4 thick ML film (lower).

total film thickness ( $N =$  number of monolayers),  $\phi(E)$  is the total phase shift resulting from the  $\text{IrO}_2/\text{vacuum}$  and  $\text{IrO}_2/\text{TiO}_2$  interfaces, and  $n$  is the quantum number. Excellent agreement with the data is obtained for an empirical fit to the phase of the form  $\phi(E) = 4E$  ( $E$  in units of eV,  $\phi$  in radians).

Closer examination of the subbands reveals that, while the subbands furthest away from the Fermi energy (0 eV) are quite dispersive, those closer to the Fermi energy have much narrower bandwidths and hence have enhanced effective mass. To quantify the mass enhancement, we note that the subbands exhibit nonparabolic dispersions, and many are quite deep in binding energy, with band bottoms near 1 eV. Therefore, the simple definition of effective mass as the second derivative of the energy with respect to momentum, commonly used for low-density semiconductors, is not appropriate. To capture the mass

relevant to near-Fermi level carriers, we employ the mass enhancement parameter

$$\tilde{M} = \frac{\partial E / \partial k}{\partial \epsilon^\alpha / \partial k} \Big|_{k=k_F^\alpha} = \frac{v_0}{v_F^\alpha}, \quad (1)$$

where  $v_0$  is the bulk  $\text{IrO}_2$  band velocity (from our GGA + SO calculation) and  $v_F^\alpha$  is the experimentally measured velocity of the subband  $\alpha$ , both evaluated at the Fermi wave vector  $k_F^\alpha$  of the subband as extracted from our EDC and MDC fits (Supplemental Material [15]). This definition is identical to the one used in Refs. [27–29] for other quantum well systems, making it ideal for direct comparison with the literature. Figure 3 (filled symbols) presents the measured subband mass enhancement, exhibiting a remarkable sixfold mass enhancement of the near- $E_F$  bands, with respect to the bulk.

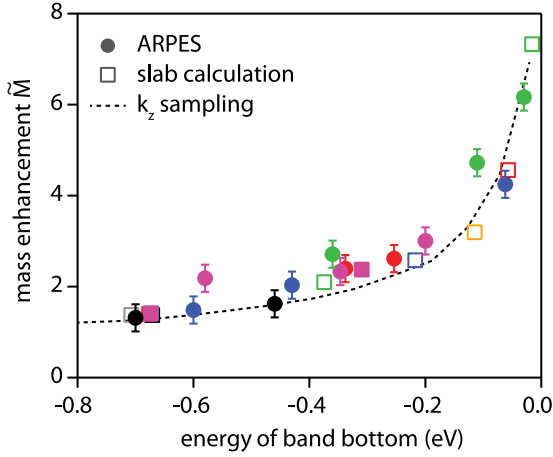


FIG. 3. Subband mass enhancement of  $\text{IrO}_2$  extracted from ARPES (solid symbols) and comparison with DFT slab calculations (open symbols) and discrete  $k_z$  sampling of the bulk dispersion (dotted line). The color coding by subband index is the same as used in Fig. 2(d).

Our measurements for  $\text{IrO}_2$  lie in striking contrast to nearly all other quantum well systems investigated to date, such as  $\text{Ag}/\text{Cu}(111)$  [5],  $\text{Au}/\text{Ag}(111)$  [4],  $\text{GaAs}/\text{AlGaAs}$  [1,2],  $\text{InAs}(001)$  [3], and  $\text{SrTiO}_3(001)$  [30,31], for which the effective mass is weakly dependent (changes of order  $\sim 10\%$ ) on subband index or film thickness. The exceptions to this are low-density  $\text{GaAs}/\text{AlGaAs}$  heterostructures [32] and  $\text{SrVO}_3$  ultrathin films [28], where in both cases, strong electron-electron interactions in the low-dimensional limit were invoked to explain the mass enhancements. For  $\text{SrVO}_3$ , the reported mass enhancement was  $\tilde{M} \approx 5$ , using the same definition we use in Eq. (1) [27–29]. While electron correlations are indeed responsible for many emergent electronic and magnetic properties found in quantum materials, they also pose a barrier towards the deterministic design of devices and applications since the most common theoretical approaches such as density functional theory do not treat these correlations accurately. Indeed, the mass enhancements reported in  $\text{GaAs}/\text{AlGaAs}$  and  $\text{SrVO}_3$  quantum wells cannot be explained using *ab initio* approaches, limiting their utility for engineering device applications.

As  $\text{IrO}_2$  is also a transition metal oxide whose near- $E_F$  states are comprised of partially filled  $d$  orbitals with strong spin-orbit coupling, it may be natural to assume that the large effective masses observed in the near- $E_F$  subbands are also due to strong electron correlations, as in the case of ultrahigh mobility  $\text{GaAs}/\text{AlGaAs}$  [32] and the correlated metal  $\text{SrVO}_3$  [28,29]. Indeed, in  $\text{IrO}_2$ , the iridium are coordinated in  $\text{IrO}_6$  octahedra with a formally  $\text{Ir}^{4+}$  valence, just like in compounds such as  $\text{Sr}_2\text{IrO}_4$ , where the combination of electron correlations from the Ir  $d$  orbitals and spin-orbit coupling give rise to a spin-orbit assisted Mott insulating state [33,34], antiferromagnetism [35],

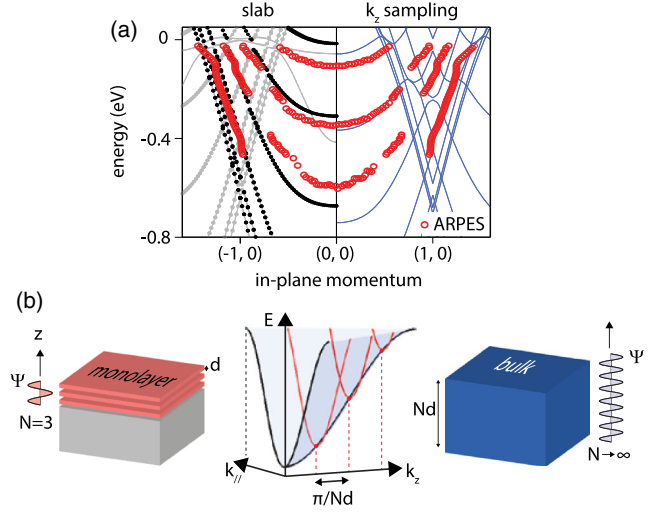


FIG. 4. Origin of mass enhancement. (a) ARPES dispersions for the 7.5 ML thick film (red circles) and comparison with a GGA + SO slab calculation for 8 ML thick  $\text{IrO}_2$  (left, black symbols) and discrete  $k_z$  sampling of the GGA + SO bulk calculation (right, blue curves). (b) Schematic of how quantized subbands ( $E$  versus  $k_{\parallel}$ ) arise from discrete  $k_z$  sampling of the bulk dispersion  $E(k_{\parallel}, k_z)$ . Sampling of  $k_z$  is in increments of  $\pi/(Nd)$ , where  $N$  is the number of monolayers and  $d = d_{110}$  is the monolayer spacing.

broken symmetry states [36,37], and the possibility of unconventional superconductivity [36–40]. On the other hand, recent ARPES studies of bulk  $\text{IrO}_2$  demonstrated surprisingly good agreement between experiment and DFT calculations [19], suggesting that the electron correlations are relatively weak, in contrast to many other perovskite iridates.

To investigate whether these unusually large mass enhancements arise from electron correlations or other effects, we compare the experimental data to DFT slab calculations including spin-orbit coupling of thin  $\text{IrO}_2$  films grown on (110)  $\text{TiO}_2$ . In Fig. 4(a), we show a comparison between the slab calculation for an 8 ML thick film (left, black symbols) and the extracted ARPES dispersions (red circles) for the 7.5 ML thick  $\text{IrO}_2$  film, which show remarkable agreement. This suggests that electron-electron interactions are not responsible for this large subband-dependent mass enhancement, since the DFT calculations do not include any explicit local correlations ( $U = 0$ ). In Fig. 3, we show a summary of  $\tilde{M}$  as a function of the band bottom energy for all the subbands measured in all of our thin films, together with a comparison from DFT slab calculations ranging between thicknesses of 2 and 10 ML, demonstrating good universal agreement. This implies that DFT-based approaches can be reliably employed to design  $\text{IrO}_2$ -based quantum well systems with engineered subband-dependent electronic properties. To our knowledge, this strong dependence of the subband effective mass with band filling is unprecedented, in the sense that this effect

can be explained without the need for invoking either strong electron correlations [27–29,41] or interactions with the substrate [42–44].

We now show that the strong dependence of the subband effective mass arises when the band structure of bulk  $\text{IrO}_2$  is quantized in the out-of-plane direction due to the finite film thickness. In contrast with simple metals such as Au (Ag) and low-density semiconductors such as GaAs, the near-Fermi energy bulk electronic structure of  $\text{IrO}_2$  is highly nonparabolic. When considering the effect of quantum confinement, for a film with a finite thickness of  $N$  atomic layers,  $k_z$  cannot be considered a continuous quantum number, but rather is discretized into  $N$  values [Fig. 4(b)]. In a simple picture, each subband samples one of those discrete  $k_z$  values, in intervals of  $\Delta k_z = \pi/(Nd)$ , such that the in-plane electronic structure of each subband is approximately a  $k_x - k_y$  slice through the bulk electronic structure at a particular  $k_z$  value.

To illustrate the effect of  $k_z$  sampling, in Fig. 4(a) we compare our ARPES measurement and DFT slab calculation for an  $N = 8$  ML thick film to a bulk calculation of  $\text{IrO}_2$  where  $k_z$  is shown every  $\pi/(Nd)$  interval (right side, blue curves). The in-plane mass enhancement extracted from  $k_z$  sampling of the bulk is plotted in Fig. 3 (dotted curve). The remarkable agreement between the ARPES data, the slab calculation, and the  $k_z$ -sampled calculation indicate that the strong subband dependence of the effective mass arises purely from quantum confinement of a nonparabolic band, without any appreciable substrate-film interactions or electron-electron correlations. In contrast,  $k_z$  discretization of a parabolic band  $E(\mathbf{k}) \sim \mathbf{kM}^{-1}\mathbf{k}^T$ , where  $\mathbf{M}$  is the effective mass tensor and  $\mathbf{k} = (k_x, k_y, k_z)$ , recovers the simple behavior of effective mass being independent of the subband ( $k_z$ ) index.

In summary, using a combination of MBE and ARPES, we discovered that the effective mass of quantum well subbands in atomically thin  $\text{IrO}_2$  films is energy dependent, with masses for the shallowest subbands enhanced as large as six times with respect to the bulk. This dramatic mass enhancement is far greater than observed in nearly any other material studied to date. By comparing the experimental data with density functional theory calculations of both finite slabs and bulk  $\text{IrO}_2$ , we determine that the origin for this effect is the highly nonparabolic electronic structure of  $\text{IrO}_2$ , which we speculate might arise from higher order hopping terms in the highly connected rutile structure. Quantum confinement in ultrathin films discretizes the out-of-plane band structure, giving rise to the observed phenomena reported here. This large mass enhancement can be accurately predicted from the bulk electronic structure and does not depend on either complex substrate-film interactions or many-body electron-electron interactions, both of which can be very difficult to treat accurately. This suggests that careful consideration of the bulk electronic structure can be used to predict and engineer quantum well

subbands with designer electronic properties. Potential applications include tunnel diodes with precisely tuned transmission current profiles (which depend both on energy level spacings and the effective masses), photocatalysts with precisely tuned kinetics (via tunable adsorbate-metal  $d$  and  $s$  band overlap [9]), and increased spin Hall voltages for enhanced spin current detection (via increased electrical resistivity, without the introduction of impurities) [11].

We thank Masaki Uchida and Yang Liu for helpful discussions. This work was primarily supported by the National Science Foundation through the Platform for the Accelerated Realization, Analysis, and Discovery of Interface Materials (PARADIM; DMR-1539918), the Air Force Office of Scientific Research (Grants No. FA9550-12-1-0335 and No. FA2386-12-1-3103), and the Gordon and Betty Moore Foundation as part of the EPiQS initiative (GBMF3850). This research also utilized shared facilities supported by the Cornell Center for Materials Research through the MRSEC program (NSF DMR-1120296) and the Cornell Nanoscale Facility (Grant No. EECs-1542081), a member of the National Nanotechnology Coordinated Infrastructure. J. N. N. acknowledges support from the NSF Graduate Research Fellowship under Grant No. DGE-1650441.

---

\*Present address: Department of Materials Science and Engineering, University of Wisconsin, Madison, Wisconsin 53706, USA.

†kmshe@cornell.edu

- [1] A. T. Hatke, M. A. Zudov, J. D. Watson, M. J. Manfra, L. N. Pfeiffer, and K. W. West, *Phys. Rev. B* **87**, 161307 (2013).
- [2] L. Smrčka, P. Vašek, J. Koláček, T. Jungwirth, and M. Cukr, *Phys. Rev. B* **51**, 18011 (1995).
- [3] N. Olszowska, J. Lis, P. Ciochon, L. Walczak, E. G. Michel, and J. J. Kolodziej, *Phys. Rev. B* **94**, 115305 (2016).
- [4] T.-C. Chiang, *Surf. Sci. Rep.* **39**, 181 (2000).
- [5] M. A. Mueller, T. Miller, and T.-C. Chiang, *Phys. Rev. B* **41**, 5214 (1990).
- [6] J. Paggel, T. Miller, D.-A. Luh, and T.-C. Chiang, *Appl. Surf. Sci.* **162–163**, 78 (2000).
- [7] C. Gmachl, F. Capasso, D. L. Sivco, and A. Y. Cho, *Rep. Prog. Phys.* **64**, 1533 (2001).
- [8] M. Sweeny and J. Xu, *Appl. Phys. Lett.* **54**, 546 (1989).
- [9] B. Hammer and J. K. Nørskov, *Adv. Catal.* **45**, 71 (2000).
- [10] H. Hwang, Y. Iwasa, M. Kawasaki, B. Keimer, N. Nagaosa, and Y. Tokura, *Nat. Mater.* **11**, 103 (2012).
- [11] K. Fujiwara, Y. Fukuma, J. Matsuno, H. Idzuchi, Y. Niimi, Y. Otani, and H. Takagi, *Nat. Commun.* **4** (2013).
- [12] D.-Y. Kuo, J. K. Kawasaki, J. N. Nelson, J. Kloppenburg, G. Hautier, K. M. Shen, D. G. Schlom, and J. Suntivich, *J. Am. Chem. Soc.* **139**, 3473 (2017).
- [13] C. E. Dreyer, A. Janotti, and C. G. Van de Walle, *Appl. Phys. Lett.* **102**, 142105 (2013).
- [14] S.-H. Park, *J. Appl. Phys.* **91**, 9904 (2002).
- [15] See Supplemental Material at <http://link.aps.org/supplemental/10.1103/PhysRevLett.121.176802> for details

- on sample growth and ARPES fitting, which includes Refs [16–18].
- [16] W. Ryden, A. Lawson, and C. Sartain, *Phys. Lett.* **26A**, 209 (1968).
- [17] A. Lanzara, P. Bogdanov, X. Zhou, S. Kellar, D. Feng, E. Lu, T. Yoshida, H. Eisaki, A. Fujimori, K. Kishio *et al.*, *Nature (London)* **412**, 510 (2001).
- [18] Z. Zhong, Q. Zhang, and K. Held, *Phys. Rev. B* **88**, 125401 (2013).
- [19] J. K. Kawasaki, M. Uchida, H. Paik, D. G. Schlom, and K. M. Shen, *Phys. Rev. B* **94**, 121104 (2016).
- [20] J. K. Kawasaki, D. Baek, H. Paik, H. P. Nair, L. F. Kourkoutis, D. G. Schlom, and K. M. Shen, *Phys. Rev. Mater.* **2**, 054206 (2018).
- [21] M. Izumi, Y. Ogimoto, Y. Okimoto, T. Manako, P. Ahmet, K. Nakajima, T. Chikyow, M. Kawasaki, and Y. Tokura, *Phys. Rev. B* **64**, 064429 (2001).
- [22] D. Toyota, I. Ohkubo, H. Kumigashira, M. Oshima, T. Ohnishi, M. Lippmaa, M. Takizawa, A. Fujimori, K. Ono, M. Kawasaki *et al.*, *Appl. Phys. Lett.* **87**, 162508 (2005).
- [23] W. J. Kim, S. Y. Kim, C. H. Kim, C. H. Sohn, O. B. Korneta, S. C. Chae, and T. W. Noh, *Phys. Rev. B* **93**, 045104 (2016).
- [24] X. Hou, R. Takahashi, T. Yamamoto, and M. Lippmaa, *J. Cryst. Growth* **462**, 24 (2017).
- [25] M. El Khakani, M. Chaker, and E. Gat, *Appl. Phys. Lett.* **69**, 2027 (1996).
- [26] T. Miller, A. Samsavar, G. E. Franklin, and T.-C. Chiang, *Phys. Rev. Lett.* **61**, 1404 (1988).
- [27] S. Okamoto, *Phys. Rev. B* **84**, 201305 (2011).
- [28] K. Yoshimatsu, K. Horiba, H. Kumigashira, T. Yoshida, A. Fujimori, and M. Oshima, *Science* **333**, 319 (2011).
- [29] M. Kobayashi, K. Yoshimatsu, E. Sakai, M. Kitamura, K. Horiba, A. Fujimori, and H. Kumigashira, *Phys. Rev. Lett.* **115**, 076801 (2015).
- [30] W. Meevasana, P. King, R. He, S. Mo, M. Hashimoto, A. Tamai, P. Songsiririthigul, F. Baumberger, and Z. Shen, *Nat. Mater.* **10**, 114 (2011).
- [31] A. Santander-Syro, O. Copie, T. Kondo, F. Fortuna, S. Pailhes, R. Weht, X. Qiu, F. Bertran, A. Nicolaou, A. Taleb-Ibrahimi *et al.*, *Nature (London)* **469**, 189 (2011).
- [32] Y.-W. Tan, J. Zhu, H. L. Stormer, L. N. Pfeiffer, K. W. Baldwin, and K. W. West, *Phys. Rev. Lett.* **94**, 016405 (2005).
- [33] B. Kim, H. Jin, S. Moon, J.-Y. Kim, B.-G. Park, C. Leem, J. Yu, T. Noh, C. Kim, S.-J. Oh *et al.*, *Phys. Rev. Lett.* **101**, 076402 (2008).
- [34] G. Jackeli and G. Khaliullin, *Phys. Rev. Lett.* **102**, 017205 (2009).
- [35] J. Matsuno, K. Ihara, S. Yamamura, H. Wadati, K. Ishii, V. Shankar, H.-Y. Kee, and H. Takagi, *Phys. Rev. Lett.* **114**, 247209 (2015).
- [36] Y. Kim, O. Krupin, J. Denlinger, A. Bostwick, E. Rotenberg, Q. Zhao, J. Mitchell, J. Allen, and B. Kim, *Science* **345**, 187 (2014).
- [37] Y. Kim, N. Sung, J. Denlinger, and B. Kim, *Nat. Phys.* **12**, 37 (2016).
- [38] H. Watanabe, T. Shirakawa, and S. Yunoki, *Phys. Rev. Lett.* **110**, 027002 (2013).
- [39] F. Wang and T. Senthil, *Phys. Rev. Lett.* **106**, 136402 (2011).
- [40] Y. J. Yan, M. Q. Ren, H. C. Xu, B. P. Xie, R. Tao, H. Y. Choi, N. Lee, Y. J. Choi, T. Zhang, and D. L. Feng, *Phys. Rev. X* **5**, 041018 (2015).
- [41] J. H. Dil, J. W. Kim, T. Kampen, K. Horn, and A. R. H. F. Ettema, *Phys. Rev. B* **73**, 161308 (2006).
- [42] S.-J. Tang, C.-Y. Lee, C.-C. Huang, T.-R. Chang, C.-M. Cheng, K.-D. Tsuei, and H.-T. Jeng, *Appl. Phys. Lett.* **96**, 103106 (2010).
- [43] B. Slomski, F. Meier, J. Osterwalder, and J. H. Dil, *Phys. Rev. B* **83**, 035409 (2011).
- [44] Y. Liu, J. J. Paggel, M. H. Upton, T. Miller, and T.-C. Chiang, *Phys. Rev. B* **78**, 235437 (2008).

# Supplemental: Engineering Carrier Effective Masses in Ultrathin Quantum Wells of IrO<sub>2</sub>

Jason K. Kawasaki,<sup>1,2,\*</sup> Choong H. Kim,<sup>3</sup> Jocienne N. Nelson,<sup>2</sup> Sophie Crisp,<sup>2</sup> Christian J. Zollner,<sup>4</sup> Eric Biegenwald,<sup>5</sup> John T. Heron,<sup>5</sup> Craig J. Fennie,<sup>4</sup> Darrell G. Schlom,<sup>1,5</sup> and Kyle M. Shen<sup>1,2,†</sup>

<sup>1</sup>*Kavli Institute at Cornell for Nanoscale Science, Cornell University, Ithaca NY 14853*

<sup>2</sup>*Laboratory for Atomic and Solid State Physics, Cornell University, Ithaca NY 14853*

<sup>3</sup>*Seoul National University*

<sup>4</sup>*Department of Applied and Engineering Physics, Cornell University, Ithaca NY 14853*

<sup>5</sup>*Department of Materials Science and Engineering, Cornell University, Ithaca NY 14853*

(Dated: October 3, 2018)

**MBE growth.** Atomically smooth (110) IrO<sub>2</sub> films with the rutile polymorph were grown on (110)-oriented single-crystal substrates of TiO<sub>2</sub> by MBE using an electron beam evaporator for iridium and distilled ozone as the oxidant (background pressure 10<sup>-6</sup> torr). Atomic fluxes were calibrated by a quartz crystal microbalance (QCM) immediately prior to growth, and film growth rates measured by reflection high-energy electron diffraction (RHEED) intensity oscillations during growth. The thicknesses extracted from the fringe periodicity agree with the thickness deduced from reflection high-energy electron diffraction (RHEED) oscillations. At 275 °C, IrO<sub>2</sub> grows in a layer-by-layer mode, resulting in oscillations of the RHEED intensity in which one period corresponds to 1 monolayer (ML,  $d_{110} = 3.2$  Å) of growth, enabling the precise control of thickness in real time. We restrict our analysis to films of thickness 3 ML or greater, which are all smooth and two-dimensional as indicated by a sharp arc of spots in the RHEED pattern. Below this limit the films typically showed atomic scale roughness as indicated by a slight spottiness of the RHEED patterns. We attribute the roughness during the first 2 ML of growth to the large lattice mismatch between IrO<sub>2</sub> and the TiO<sub>2</sub> substrate (1.8% tensile along [001] and 3.8% compressive along [1 $\bar{1}$ 0]). A sharp arc of spots and smooth film growth is recovered by the third monolayer. The highest quality samples were produced via growth at a low growth temperature (275 °C) followed by a higher temperature (400 °C) *in situ* anneal under the same pressure of distilled ozone.

**In-situ ARPES.** Immediately following growth, samples were transferred through ultrahigh vacuum within 300 seconds to an ARPES chamber equipped with a Scienta R4000 analyzer, monochromated helium plasma discharge lamp, and low-energy electron diffraction (LEED) system. ARPES measurements were performed at a temperature of 20 K with an energy resolution of  $\Delta E = 11$  meV and a chamber base pressure of  $4 \times 10^{-11}$  Torr.

**Ex-situ structural characterization.** Following ARPES measurements, samples were characterized by *ex situ*  $\theta - 2\theta$  x-ray diffraction (Cu  $K\alpha$ ), and atomic force microscopy. For the  $\theta - 2\theta$  XRD scans (Fig. 1a of the main manuscript), in addition to the 110 and

220 Bragg reflections at 27.9 and 57.8 degrees, respectively, we observe sharp and persistent finite thickness (Kiessig) fringes, resulting from strong interference between top and bottom interfaces. The presence of such well-resolved fringes indicates flat surfaces and a sharp IrO<sub>2</sub>/TiO<sub>2</sub> interfaces, and the thicknesses extracted from the measured fringe periodicity is within 0.5 ML of the thickness expected from RHEED oscillations. X-ray rocking curve measurements are similarly sharp with typical full width at half maximum (fwhm) of the film reflections ranging from 20 to 35 arc seconds, similar in magnitude to fwhm of 15-30 arc seconds for the substrate. Further details of growth and characterization for bulk-like samples are provided elsewhere [1, 2].

**Magnetotransport.** Magnetotransport measurements were performed in a Quantum Design Physical Properties Measurements System. The residual resistivity (4 Kelvin) of 4  $\mu\Omega$ -cm for the bulk-like 50 ML film is the lowest of any epitaxial IrO<sub>2</sub> film to date, and the resistivity of the ultrathin films is similarly low (Fig. S-1a). All films showed a linear dependence of transverse (Hall) voltage  $V_{xy}$  versus magnetic field out to 5 Tesla, with a positive (hole-like) Hall coefficient  $R_H$ . However, we note that due to the multiband character of IrO<sub>2</sub>, the carrier density extracted as  $n_{2d} = 1/R_H q$  should only be viewed as an *effective* density. We also find that the slope of  $R_H$  versus temperature changes sign for films thinner than 10 ML (main text Fig. 1e). This critical thickness behavior near 10 ML also manifests in plots of the low temperature (4 K) effective three-dimensional density versus thickness (Fig. S-1b), for which films below the 10 ML limit show a rapid decrease in density. We attribute these general trends to a the complex multi-band character of IrO<sub>2</sub>.

**Valence band dispersion.** ARPES measurement ( $k_y = 0$ ) of the valence band for the 50 ML sample, and comparison to the GGA+SO calculation for constant  $k_z = 0.76\pi/d_{110}$ , as determined from a free-electron-like model of final states [1] (Fig. S-2a). Due to the half periodicity of the unreconstructed (110) surface Brillouin zone with respect to that of the bulk (Fig. S-2b), zone folded bands appear in the ARPES measurement from surface Umklapp scattering.

**EDCs, MDCs, and dispersion fitting.** Raw en-

ergy dispersion curves (EDCs) are shown in Fig. S-3, exhibiting quasiparticle peaks with typical fwhm (full width at half maximum) of 0.05 – 0.1 eV for binding energies within 0.5 eV of the Fermi energy. Typical MDC widths at the Fermi energy are  $\Delta k = 0.1 - 0.15 \text{ \AA}^{-1}$ . Measurements using He I ( $h\nu = 21.2 \text{ eV}$ , bottom row) and He II ( $h\nu = 40.8 \text{ eV}$ , top row) exhibit nearly identical dispersions, confirming the two-dimensional nature of the sub-bands. The corresponding color intensity plots are shown in the main text Fig. 2 (He I excitation) and Fig. S-4 (He II excitation). Dispersions near the band bottoms were extracted from the peak positions of Lorentzian fits to the EDCs, with a smooth second-order polynomial background convolved with the Fermi-Dirac distribution. Dispersions near the Fermi energy were extracted from momentum distribution curve fits (MDC, intensity versus angle at constant binding energy), using Lorentzians and a smooth second order polynomial background.

**Extracting the Fermi velocity.** In general,  $v_F^\alpha$  was extracted from a linear fit to the momentum distribution curve (MDC)-extracted dispersion, within 100 meV of the Fermi energy. We note, however, that for the 50 ML thick sample and for the  $n = 1$  sub-band of the 9 ML and 7.5 ML thick samples, a kink is observed in the dispersion at a binding energy of approximately 80 meV (Fig. 4 main text). We attribute this kink to electron-boson coupling, as has been observed in other systems such as the cuprates [3]. This energy scale is similar to that of the Debye temperature of  $\text{IrO}_2$  ( $k_B\theta_D \approx 60 \text{ meV}$  [4]). For these few kinked sub-bands, the Fermi velocity was extracted from the pre-kink region, i.e. binding energy of 100 – 200 meV, since for uniform comparison across the sub-bands we are primarily interested in electronic contributions to the effective mass.

**DFT.** Density functional theory calculations were performed using the generalized gradient approximation and fully relativistic spin-orbit coupling (GGA+SO) in WIEN2K and VASP. The bulk dispersion is shown in Fig. S-5(a).

**Tight binding model.** Rutile  $\text{IrO}_2$  is composed of both edge- and corner-sharing  $\text{IrO}_6$  octahedra, which produces significant higher order hopping terms in the out-of-plane direction, and even significant direct Ir-Ir

bonding. Our two-band tight binding model consists of one  $5d$  orbital at each Ir site (Fig. S-5). We define  $t(\frac{1}{2}, \frac{1}{2}, \frac{1}{2})$  as the  $M - O - M$  oxygen-mediated hopping between corner-sharing  $\text{IrO}_6$  octahedra ( $M = \text{transition metal}$ ),  $t_c(0, 0, 1)$  as the direct  $M - M$  hopping between edge-sharing octahedra along the conventional  $c$ -axis, and  $t_a(1, 0, 0)$  as the second-nearest neighbor hopping along the conventional  $a$ -axis. An excellent fit to the bulk GGA+SO calculation is found for  $t_c/t = 0.63$  (direct  $M - M$ ),  $t_a/t = 0.44$  (next nearest neighbor), and  $t = -0.8 \text{ eV}$ , demonstrating a strong relative weight of these higher order hoppings.

In contrast, for previously investigated quantum well materials such as the perovskite  $\text{SrVO}_3$ , the hopping terms in the all-corner-shared network are dominated by the nearest neighbor  $180^\circ M - O - M$  interactions  $t$  and the higher order interactions are much less significant:  $t_{ab}/t = 0.08$  and  $t_{2a}/t = 0.03$ , where  $t_{ab}(1, 1, 0)$  is second-nearest neighbor, and  $t_{2a}(2, 0, 0)$  is the third-nearest neighbor [5] interaction. The large, three-dimensional, higher order hopping interactions for  $\text{IrO}_2$  also lie in stark contrast with noble metals (e.g., Cu, Ag) where the electronic structure is effectively free-electron-like. These higher-order hopping terms in bulk  $\text{IrO}_2$  result in an electronic structure that is highly non-parabolic.

---

\* Current address: Department of Materials Science and Engineering, University of Wisconsin, Madison WI 53706  
 † kmshen@cornell.edu

- [1] J. K. Kawasaki, M. Uchida, H. Paik, D. G. Schlom, and K. M. Shen, Phys. Rev. B **94**, 121104 (2016), URL <http://link.aps.org/doi/10.1103/PhysRevB.94.121104>.
- [2] J. K. Kawasaki, D. Baek, H. Paik, H. P. Nair, L. F. Kourkoutis, D. G. Schlom, and K. M. Shen, Phys. Rev. Materials **2**, 054206 (2018), URL <https://link.aps.org/doi/10.1103/PhysRevMaterials.2.054206>.
- [3] A. Lanzara, P. Bogdanov, X. Zhou, S. Kellar, D. Feng, E. Lu, T. Yoshida, H. Eisaki, A. Fujimori, K. Kishio, et al., Nature **412**, 510 (2001).
- [4] W. Ryden, A. Lawson, and C. Sartain, Physics Letters A **26**, 209 (1968).
- [5] Z. Zhong, Q. Zhang, and K. Held, Phys. Rev. B **88**, 125401 (2013), URL <https://link.aps.org/doi/10.1103/PhysRevB.88.125401>.

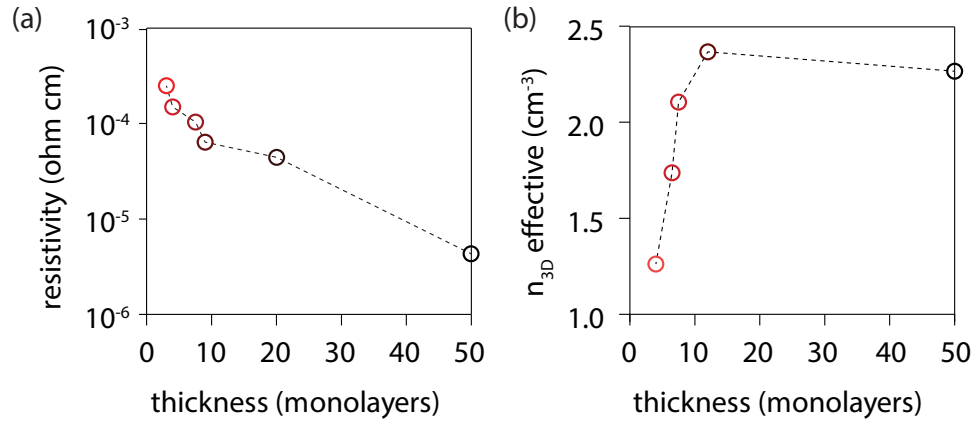


FIG. S-1. Thickness-normalized transport properties of ultrathin (110) IrO<sub>2</sub> films at 5 K. (a) The [001] resistivity decreases monotonically with film thickness. (b) The effective three-dimensional carrier density decreases sharply for films thinner than 10 ML.

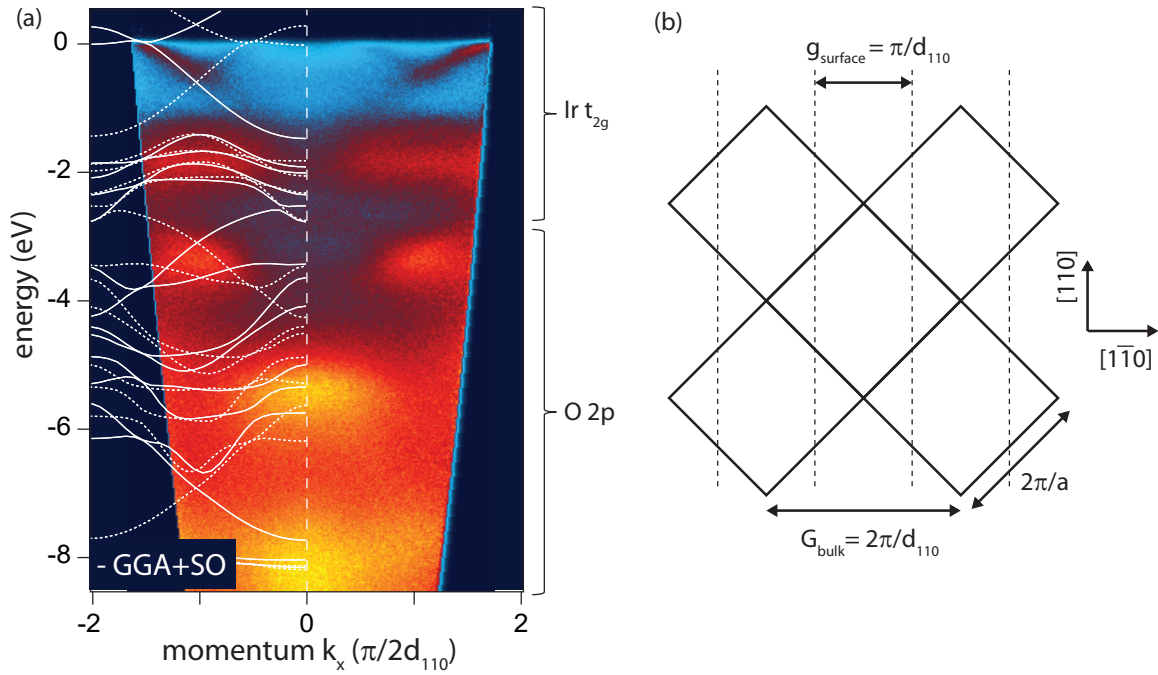


FIG. S-2. ARPES of the bulk valence band and comparison with theory. (a) High binding energy ARPES measurement ( $k_y = 0$ ) for the 50 ML sample (He I excitation), and comparison to the GGA+SO calculation for constant  $k_z = 0.76\pi/d_{110}$ , as determined from a free-electron-like model of final states [1]. Dotted and solid curves represent the original and zone-folded bands, respectively. (b) Schematic of the bulk and (110) surface Brillouin zones, highlighting the fact that the (unreconstructed) surface has half the periodicity of the bulk.

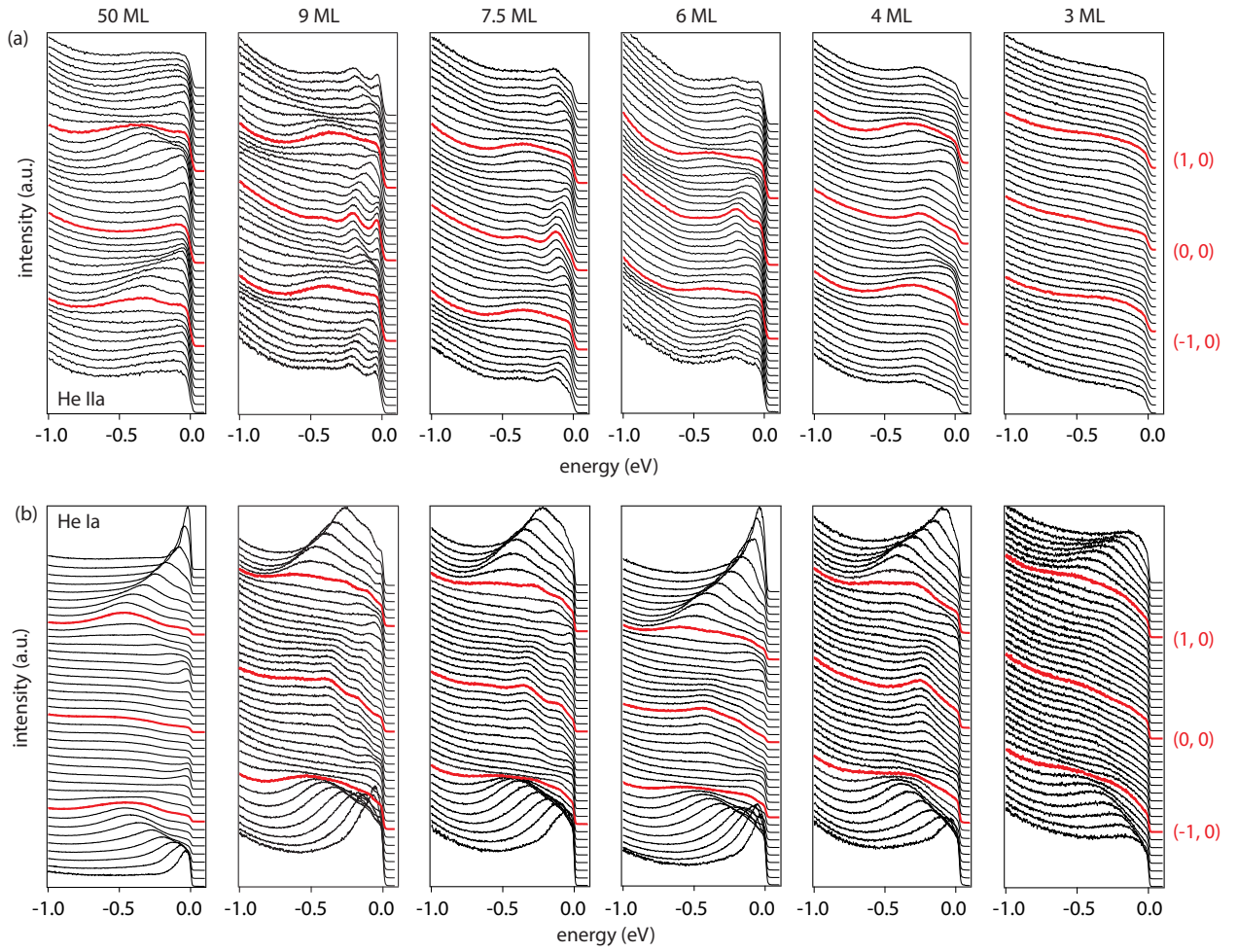


FIG. S-3. Raw ARPES energy dispersion curves for the IrO<sub>2</sub> films shown in the main text Fig. 2(a), measured at two different incident photon energies: (a)  $h\nu = 40.8$  eV (He II $\alpha$  emission), (b)  $h\nu = 21.2$  eV (He I $\alpha$ ).

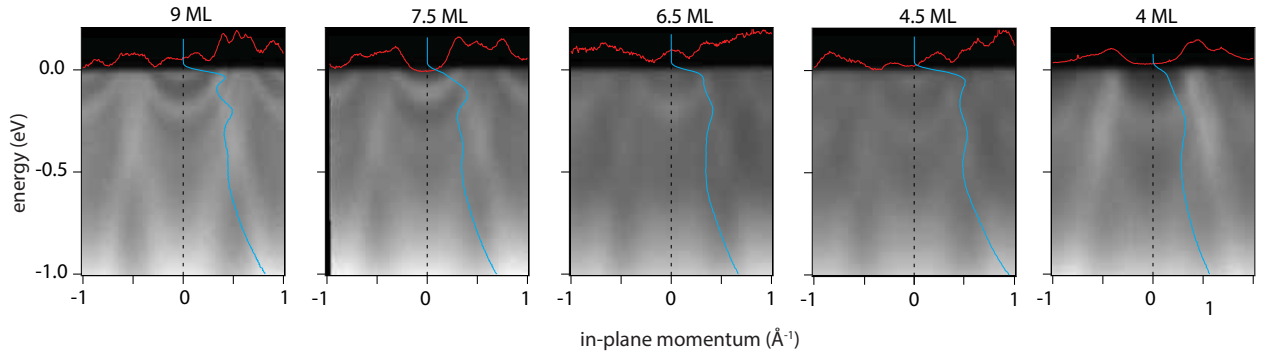


FIG. S-4. ARPES measurements using He II $\alpha$  ( $h\nu = 40.8$  eV). Blue curves are the EDCs at  $k_{\parallel} = 0$ , red curves are MDCs at the Fermi energy.

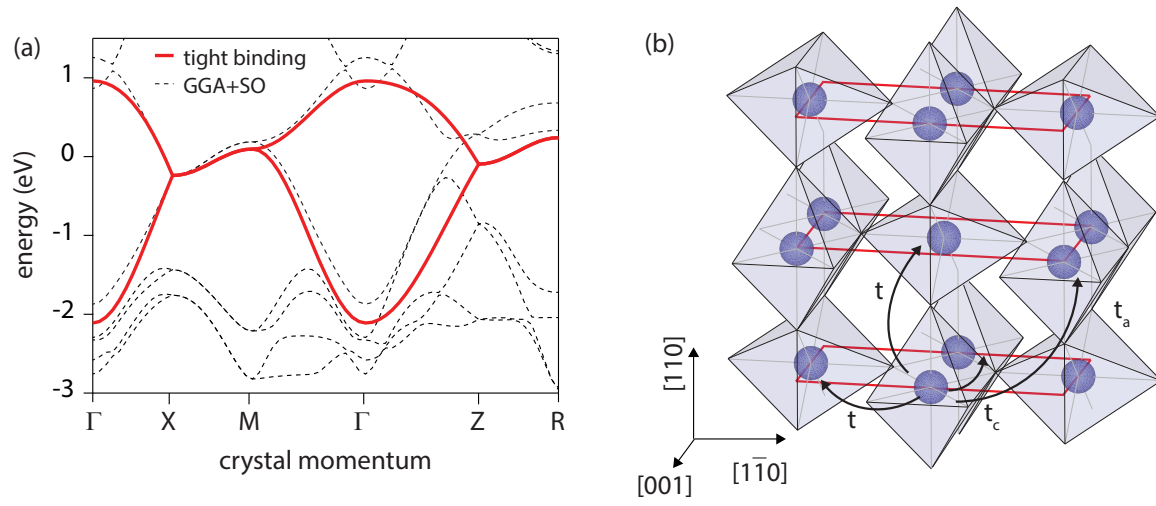


FIG. S-5. Tight binding model. (a) Two-band tight binding fit to  $\text{IrO}_2$ , for  $t = -0.8$  eV,  $t_c/t = 0.63$ ,  $t_a/t = 0.44$ , and comparison to GGA+SO. (b) Unit cell and definition of the hopping parameters. Iridium atoms are represented by the blue spheres, oxygen atoms are located at the octahedral vertices.